International Journal of Machine Tools & Manufacture 190 (2023) 104049

Contents lists available at ScienceDirect

International Journal of Machine Tools and Manufacture

journal homepage: www.elsevier.com/locate/ijmactool

In situ monitoring the effects of Ti6Al4V powder oxidation during laser powder bed fusion additive manufacturing

Gowtham Soundarapandiyan [a,c], Chu Lun Alex Leung [d,e,*], Carol Johnston [b], Bo Chen [c,f], Raja H.U. Khan [b], Phil McNutt [b], Alisha Bhatt [d,e], Robert C. Atwood [g], Peter D. Lee [d,e], Michael E. Fitzpatrick [c]

[a] National Structural Integrity Research Centre (NSIRC), Granta Park, Cambridge, CB21 6AL, UK
[b] TWI Ltd, Granta Park, Cambridge, CB21 6AL, UK
[c] Faculty of Engineering, Environment and Computing, Coventry University, Coventry, CV1 5FB, UK
[d] Department of Mechanical Engineering, University College London, WC1E 7JE, UK
[e] Research Complex at Harwell, Rutherford Appleton Laboratory, Harwell, Didcot, OX11 0FA, UK
[f] School of Engineering, University of Leicester, Leicester, LE1 7RH, UK
[g] Diamond Light Source Ltd, Harwell Science & Innovation Campus, Oxfordshire, OX11 0DE, UK

ARTICLE INFO

Handling Editor: Dragos Axinte

Keywords:
Additive manufacturing
Ti6Al4V
Laser powder bed fusion
Powder recycling
Powder oxidation
Process monitoring

ABSTRACT

Making laser powder bed fusion (L-PBF) additive manufacturing process sustainable requires effective powder recycling. Recycling of Ti6Al4V powder in L-PBF can lead to powder oxidation, however, such impact on laser-matter interactions, process, and defect dynamics during L-PBF are not well understood. This study reveals and quantifies the effects of processing Ti6Al4V powders with low (0.12 wt%) and high (0.40 wt%) oxygen content during multilayer thin-wall L-PBF using *in situ* high speed synchrotron X-ray imaging. Our results reveal that high oxygen content Ti6Al4V powder can reduce melt ejections, surface roughness, and defect population in the built parts. With increasing oxygen content in the part, there is an increase in microhardness due to solid solution strengthening and no significant change in the microstructure is evident.

1. Introduction

Additive manufacturing (AM) has attracted considerable attention in several industries and is a new paradigm for smart manufacturing, providing great commercial opportunities for the Industry 4.0 era [1,2]. Compared to conventional manufacturing methods, AM offers huge economic benefits, a high buy-to-fly ratio of 1:1.5, and geometrical freedom, allowing manufacturing of complex 3D parts directly from the raw material without tools or dies [3]. Laser powder bed fusion (L-PBF) is one of the most used metal AM processes which uses a laser beam to melt powder particles at pre-defined regions based on a CAD model [4]. L-PBF has already been used to fabricate several alloys including nickel [5], steel [6], titanium [7], copper [8], aluminium [9], *etc.* for a wide range of industrial applications. The un-melted powder is usually recycled post-manufacturing for several iterations, which makes the L-PBF process more sustainable [10]. Powder recycling offers huge economic benefits, though the physical and chemical properties of recycled powder particles may be different compared to the virgin/parent powder owing to manufacturing, handling, and storage processing steps [11]. A thorough understanding of the powder degradation mechanisms with powder recycling and their subsequent impact on the laser-matter interactions, process dynamics, and microstructure becomes critical to improve the reproducibility of L-PBF part properties.

Characterisation of recycled Ti6Al4V powder has revealed powder-particle surface deformation [12], agglomeration [13,14], changes in particle size distribution (PSD) [15], increase in humidity [12] and oxygen content [16,17]. Changes in the physical characteristics of powder particles can be detrimental to the bulk powder behaviours, *e.g.* flowability and packing behaviour, leading to poor powder layer quality and L-PBF part density [18]. Powder agglomerates can lead to lack-of-fusion defects, reducing the fatigue life of the Ti6Al4V parts [13]. Some of these internal defects could be healed by hot-isostatic pressing (HIPing) to improve the density of L-PBF parts [19,20]. Hence, the major concern on Ti6Al4V powder recyclability is the increase of powder oxygen content,

* Corresponding author. Department of Mechanical Engineering, University College London, WC1E 7JE, UK..
E-mail address: alex.leung@ucl.ac.uk (C.L.A. Leung).

https://doi.org/10.1016/j.ijmachtools.2023.104049
Received 28 December 2022; Received in revised form 7 June 2023; Accepted 8 June 2023
Available online 19 June 2023

which limits the number of times the powder can be recycled.

Ti6Al4V is highly oxidising at elevated temperatures (>450 °C). The dissolved oxygen is an interstitial element in Ti6Al4V, it can act as a strong α-phase stabiliser that improves the part strength by solid solution strengthening mechanism. The strength enhancement is caused by the restriction of dislocation movement and increase of lattice strain in the hexagonal close-packed (HCP) structure, *i.e.,* increasing the c/a ratio. When the oxygen level increases from 0.10 wt% to 0.30 wt% in Ti6Al4V material, the c/a ratio increases from 1.595 to 1.596, and as a result the micro-hardness increases significantly from 325 HV to 375 HV (average of 10 measurements at 0.5 Kg load) [21]. The increase in hardness and strength is generally compromised by a decrease in material ductility. Material elongation can reduce up to 10% with an increase of oxygen content from 0.16 wt% to 0.49 wt% due to the formation of fine $\alpha_2(Ti_3Al)$ precipitates [22].

Prior studies identified the potential sources of powder oxidation in the L-PBF process: (i) the decomposition of adsorbed moisture at the powder surface into hydrogen and oxygen during L-PBF. The dissociated oxygen leads to powder oxidation [12,23], forming TiO_2 rutile and Al_2O_3 oxides [24]. Oxidation of Ti in a humid environment occurs relatively fast due to substitutional hydroxide ion transport through the oxide scale [25]. (ii) Small concentrations of oxygen in the shielding gas may react with the powder and melt pool during L-PBF. Powder particles located closer to the melt pool had 0.03 wt% more oxygen content compared to the particles at the edges of the powder bed after 1 build cycle [13]. (iii) Melt ejections (or droplet spatter) that generate due to melt pool instabilities during L-PBF are also reported to increase the powder bed oxygen levels [26,27]. Despite these sources for powder oxidation, the oxygen content of recycled Ti6Al4V powder is within the limit of the ASTM F2924 even after 15 build cycles [28]. This is because the oxygen content of the recycled powder is generally measured by bulk measurement techniques such as inert gas fusion (IGF-IR) which measures the average oxygen content of the batch. This oversees the locally highly oxidised particles from the previous build cycles; this can lead to heterogeneity in powder layer chemistry, *i.e.,* some regions of the powder bed would have higher oxygen content compared to the rest.

Recent *ex situ* investigation [29] has shown that AM parts made from high oxygen content (0.74 wt%) regions of the powder bed exhibited low elongation of 1.1% and a reduction in area of 1.6%, resulting in brittle fracture. Heterogeneity in oxygen content could also occur within the same part, leading to premature failure from the areas containing high oxygen concentration. Besides the influence of oxygen content on metallurgical and mechanical properties, the oxide layers on the recycled powder surfaces could also affect the laser-matter interaction, the understanding of which is crucial to process and qualify parts produced from recycled Ti6Al4V powder but is as-yet missing. This forms the objective of the present work.

The advent of miniaturized AM machines that can be installed at synchrotron beamlines, coupled with hard X-ray imaging enables users to probe inside the laser-matter interaction during L-PBF at high spatiotemporal resolution. Prior *in situ* studies focused on the melt pool and keyhole dynamics [30,31], pore evolution [32,33] cracking [34], the influence of layer thickness [35] and melt pool oxidation [36,37], and multiphase interactions on the evolution of pores and surface roughness [38]. However, they merely discuss the influence of oxygen on the laser-matter interaction and subsequent phenomena during multilayer L-PBF.

Here, we used a miniaturized L-PBF machine and high-speed X-ray imaging to capture the transient phenomena during multilayer L-PBF build using virgin and oxidised powders. Our results quantified the effects of high oxygen content particles having surface oxide layers on the molten pool dynamics, spatter, surface roughness, and defects during L-PBF. Under the conditions studied, we show that L-PBF of 0.40 wt% oxidised Ti6Al4V powder can reduce defects (*e.g.,* pores), melt ejections and improve overall surface finish. In other words, Ti6Al4V powder could be intentionally oxidised to improve the L-PBF print quality, depending on the requirements of the end-use products.

2. Methodology

2.1. Powder feedstock

A commercially available argon-gas-atomised (AGA) Ti6Al4V powder supplied by TLS Technik (or Altana) was used in this study, see chemical composition in Table 1.

2.2. Powder oxidation

High oxygen content Ti6Al4V powder was prepared by artificially oxidising a virgin AGA powder using a custom-built powder heat treatment furnace (Supplementary Fig. 1). The virgin powder was poured into a stainless-steel vessel inside the furnace which consists of two parts joined together by a flange and sealed with a copper gasket. The powder was tumbled/mixed by an electroplated (to prevent contamination by wear) stirrer rotated at 10 rpm to prevent powder sintering at high temperature and ensure homogenous powder oxidation. The powder was heated to 475 °C and held for 5 h with an Ar flow rate of 0.5 l/min at 1 bar pressure, followed by furnace cooling. The oxygen level in the vessel was controlled by purging Ar gas throughout the heat treatment cycle. The temperature was monitored using a thermocouple inserted into the vessel of the furnace. The oxidised powder was sieved through a vibratory mesh of 70 μm. No sintered particles were found after checking the sieve mesh. Given that the maximum reported oxygen content of the recycled Ti6Al4V powder in prior study was 0.33 wt% [39], the aim of our oxidation experiment was to increase the powder oxygen content to ~0.40 wt%.

2.3. Powder characterisation

The oxygen contents of the virgin and oxidised powders were measured using IGF-IR spectroscopy following ASTM E1409. Five samples of oxidised powder were tested to verify the homogeneity in powder oxidation. The oxygen content of the virgin and oxidised powders measured 0.12 wt% (low) and 0.40 wt% (high), respectively.

Powder morphologies of the virgin and oxidised powders were studied using a Zeiss Sigma field-emission-gun scanning electron microscope (FEG-SEM) equipped with a backscattered electron (BSE) detector. Laser diffraction method was used to estimate the particle size distribution (PSD) (Malvern Panalytical Mastersizer 3000 system according to ASTM B822. It reported the volume of particles over the powder size range. $D_v(x)$ means that x percentage of particles of the total volume is higher or lower than a particular particle diameter. The flowability of both powders was measured by Hall flow testing following ASTM B213. Five measurements were taken per powder condition. The room temperature and humidity were about 22°C and 44%, respectively, throughout the measurements.

For the powder cross-sectional analysis, the powder particles were mounted and ground using 2500-grit SiC paper, followed by fine polishing down to 0.25 μm using diamond suspensions. The particle cross-sections were etched using Kroll's reagent (2 vol% HF, 5 vol% HNO_3, and 43 vol% H_2O) by swabbing the polished surfaces for ~20 s to reveal the microstructure. They were then examined using the BSE imaging mode. Energy dispersive spectroscopy (EDS) line scans were performed across the cross-sectional surface of both powders to quantify the oxygen elemental distribution.

The laser absorbance of the virgin and oxidised powder were

Table 1
Chemical composition (wt.%) of Ti6Al4V powder.

Al	V	N	C	O	Fe	Ti
6.370	3.980	0.010	0.015	0.120	0.182	Bal.

measured by the diffuse reflectance (R) converted into Kubelka-Munk unit, F(R), using UV-VIS-NIR spectroscopy with an integrating sphere attachment (UV-2600 and IRS-2600 plus, Shimadzu Corporation, Japan), see method section in Ref. [40]. The F(R) was used to correlate the laser absorbance of both powders.

2.4. *In situ* high-speed X-ray imaging of the L-PBF process

To understand the effects of Ti6Al4V powder oxidation on the laser-matter interaction, *in situ* X-ray imaging experiments were conducted in a miniature L-PBF rig *a.k.a. in situ* and *operando* process replicator (ISOPR) using virgin (0.12 wt% O) and oxidised (0.40 wt% O) powders. Full details of the ISOPR can be found in Ref. [37]. The ISOPR has a 200 W Yb-doped fibre laser which operates at 1070 nm wavelength in continuous wave (CW) mode, focused to 50 μm spot size at a focal distance of 254 mm via an f-theta lens. The build chamber has a sample holder that sandwiches a commercially pure titanium (CP–Ti) substrate plate between two glassy carbon plates. The substrate plate was aligned with the focal plane of the laser beam and perpendicular to the synchrotron X-rays. The glassy carbon plate allows >90% X-ray transmission at 20–150 keV [38]. For each set of experiments, a 10-layer-high thin-wall structure of 5 mm length using bi-directional scanning strategy was built by L-PBF whilst monitoring each layer by X-ray radiography. The build chamber was initially evacuated and then backfilled with Ar at 4 l/min flow rate. The powder was fed over the CP-Ti substrate base plate using a vibratory hopper. An attached blade-type re-coater levelled the deposited powder. The process parameters used for both the virgin and oxidised powders were the same. In this study, we used a laser power of 150 W, a scan speed of 50 mms^{-1}, and a layer thickness of 100 μm. A relatively high layer thickness and slow scan speed were chosen to attain a better visualisation of the physical phenomena with X-ray radiography during L-PBF.

The *in situ* X-ray imaging experiments were conducted using the I12: JEEP beamline at Diamond Light Source, UK. The mean energy of the X-ray beam was 55 keV. After interacting with the melt pool, the attenuated X-rays were converted to visible light using a 700-μm-thick LuAg: Ce scintillator and the radiographs were recorded with a CMOS camera (Miro 310 M, Vision Research, US) at 5100 frames per second (fps), a 6.6 μm pixel resolution and a field of view of 8.4 mm (width) × 3.3 mm (height), see similar imaging conditions as described in Ref. [30].

2.5. *Image processing*

Matlab R2020a and open-source software Fiji version 1.52i were used to process and analyse the obtained radiographs, following by flat-field correction (FFC) and denoising techniques described in Refs. [38, 41]. The radiographs were processed using the image processing toolbox of Matlab R2020a to improve image contrast and segmentation of the melt-pool boundary for surface roughness study. An example of the image processing stages is provided in Supplementary Fig. 2.

2.6. *Surface roughness and melt ejection measurements*

Spatter and surface roughness measurements were performed for each layer of the 10-layer build. The droplet spatters were quantified using the manual tracking plugin available in Fiji software. Melt track roughness was measured based on the X–Y pixel coordinates along the melt track boundary. To avoid the protrusion effects at the front and rear side of the melt tracks on surface roughness analysis, and to be consistent with 3D optical profilometer measurements, we quantified the mean roughness value (R_a) only in the middle part of the melt track, *i.e.,* 2 mm from the centre. Evaluating the surface roughness from X-ray radiographs is not a standardised method, and hence the final track (10th layer) roughness measurements from X-ray radiographs were compared with the 3D optical profilometer (Alicona InfiniteFocusSL) measurements based on the ISO4287 standard. As per ISO4288, the evaluation length (l_n) and sampling length (l_r) should be greater than 12.5 mm and 2.5 mm, respectively. Since the length of the melt track was only 5 mm, l_r was set to 0.8 mm and l_n was set to 4 mm, which was a slight deviation from the standard.

2.7. *X-ray computed tomography*

X-ray computed tomography (XCT) was performed on build tracks produced from virgin and oxidised powders using a laboratory-based XCT system (Nanofocus, Phoenix|X-ray) at the Research Complex at Harwell, UK. Each XCT scan was performed at 100 kV and 140 μA with a 0.34-mm-thick copper filter, comprising 1000 radiographic projections with a 1 s exposure time per projection. These projections were reconstructed via filtered back projection using Datos|x software, resulting in an image matrix of 588 × 407 × 997 pixels with a voxel size of 5.69 × 5.69 × 5.69 μm^3. The reconstructed image volume was subsequently analysed in Avizo 8.0 (Thermofisher Scientific). Firstly, the input image volume was deblurred by 3D unsharp masking, for contrast enhancement and image sharpening. Secondly, the filtered image was then binarised by interactive thresholding. The volume fraction, porosity (%), and sphericity measurements were performed according to Ref. [41].

2.8. *Microstructure and hardness*

For the microstructural investigation, the 10-layer builds were mounted and ground with SiC abrasive papers (from 360- to 2500-grits). Final polishing and etching were performed using the same method as for the powders. The microstructure along the build direction of the sample was imaged using secondary electron (SE) imaging mode in the Zeiss Sigma FEG-SEM. Hardness testing was conducted using a ZHVμ Vickers Microhardness Tester (Zwick Roell Group) following ASTM E92 on as-polished samples. Six indentations with 1 kgf and 10 s dwell time were performed in the lateral direction (perpendicular to build direction) of both samples.

3. Results

3.1. *Powder characteristics*

Most of the virgin (Fig. 1a) and oxidised (Fig. 1b) powder particles were spherical with some satellites and agglomerates that are commonly found in AGA powders. The PSD curve of the oxidised powder was slightly narrower compared to the virgin powder, a general phenomenon observed in recycled powder [28] (Fig. 1c). The $D_v(10)$, $D_v(50)$ and $D_v(90)$ values were 26, 38 and 55 μm for the virgin and 27, 38 and 54 μm for the oxidised powders, respectively. The Hall flowrate measured 31 ± 0.04 s/50 g and 30 ± 0.03 s/50 g for the virgin and oxidised powders, respectively. Both powders exhibited continuous flow without any interruptions. The marginal improvement in the flow behaviour of the oxidised powder can be attributed either to the reduction of fine particles as revealed by a slight shift towards the left side of the PSD bell curve (see Fig. 1c) or due to the possible reduction in the moisture level after heat treatment. Prior work [17,23,28,42] reported no significant degradation in powder morphology, narrowing of PSD and improvement in powder flow, similar to our observation. Overall, the changes in the powder's physical properties were only marginal, and no powder degradation was observed due to the artificial oxidation process.

Cross-sections of the virgin and oxidised powders are shown in Fig. 1d and e, respectively. The heat treatment temperature during artificial powder oxidation was maintained at 475 °C, which is well below the β-transus temperature (~990 °C) [43], hence no microstructural changes occurred and both powders consisted of α' microstructure. The SEM-EDS analysis confirmed that the oxidised powder particle had a surface oxide layer whereas no visible oxide layer was present in the virgin powder particle (Fig. 1f and g). The oxygen content measured by IGF-IR revealed 0.40 wt% O for the oxidised powder, which is >3 times

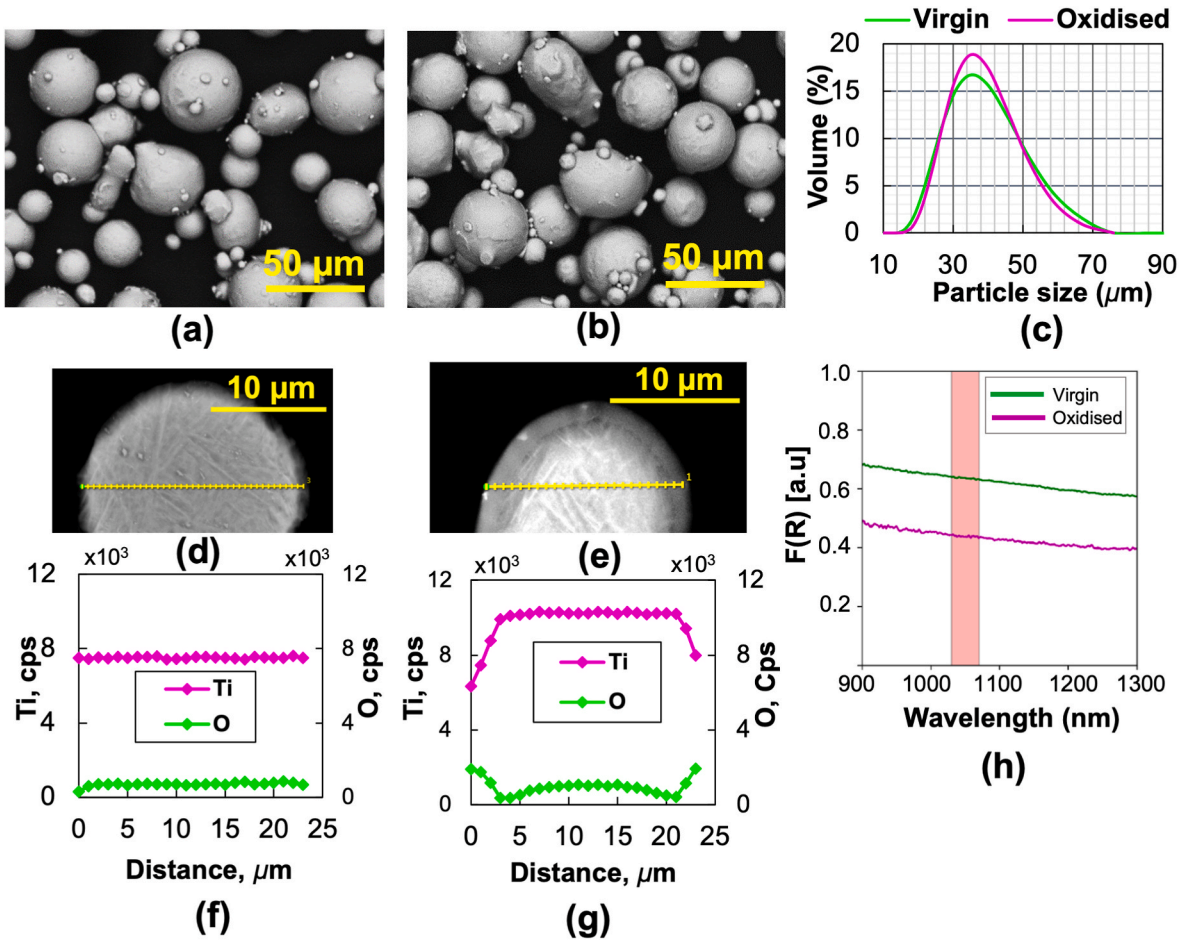

Fig. 1. SEM powder morphology BSE image of (a) virgin and (b) oxidised powder; (c) PSD bell curve of virgin and oxidised powder. Powder cross-section of a (d) virgin and (e) oxidised powder particle with their corresponding EDS line maps (f) and (g), respectively; (h) Kubelka-Munk transform, F(R), of the diffuse reflectance. The wavelength of the laser (1030–1070 nm) is indicated by the pink region. (For interpretation of the references to colour in this figure legend, the reader is referred to the Web version of this article.)

higher than the virgin powder (0.12 wt%). Since powder oxidation was performed at a low temperature, it is less likely to vaporise the light elements. Therefore, the remaining chemical elements such as aluminium and vanadium contents in the oxidised powder were assumed to be the same as the virgin powder (Table 1). The UV-VIS-NIR reflectance measurement in F(R) unit (Fig. 1h) shows that the oxidised powder had almost half the laser absorbance than the virgin powder due to the presence of surface oxide layer.

3.2. *Multi-layer build formation using virgin and oxidised powder in L-PBF process*

The time-series X-ray radiographs show the multi-layer melt track formation during L-PBF of virgin and oxidised powder feedstocks, see Figs. 2 and 3, respectively. A bi-directional scan strategy was employed, *i.e.,* the scan direction reversed after each powder layer was melted. The yellow-dashed line in the radiographs represent the local depression region that formed where the laser beam was irradiated. The vapour depression zone indicated the position of the laser beam as represented by yellow dashed-lines in the radiographs. Continuous ejection of powder and droplet spatters occurred during laser-matter interaction, as evident in the radiographs and Supplementary videos 1 - 6. The width of the substrate plate was larger than the printed melt-tracks, which allows spatter particles to deposit between the melt track and glassy carbon plates.

Supplementary video related to this article can be found at doi:10.1016/j.ijmachtools.2023.104049

We observed the formation of the agglomerated powder-spatters (D_{eq}>60 µm) at the front of the laser beam in Supplementary Fig. 3. The cluster of powder particles was first entrained in the vapour plume and then interacted with the laser beam, forming a molten droplet which continued to entrain in the Ar flow [44]. These agglomerated spatters may generate defects if they fall back into the melt pool or lower the powder recyclability when they landed onto the un-melted part of the powder bed (see discussion in Section 3.4). Most of the droplet spatters were ejected vertically from the melt pool without disturbing the un-fused powder and later entrained along the Ar flow direction throughout the 10 layer build. Some of the droplet spatters also collided with the loose particles near-by the laser-matter zone, forming a larger spatter, similar to that reported in Ref. [45].

3.3. *Droplet spatter quantification*

Due to the large pixel size of the imaging setup and the high-energy X-rays, small spatters with D_{eq}<60 µm were mostly transparent to the X-rays. Powder spatters with a D_{eq}<60 µm were not included in the spatter analysis. To avoid discrepancies in the results, we focused on the phenomena that occur at the melt pool and only analysed the droplet spatters with $D_{eq}\geq$ 60 µm. Fig. 4 shows the total number of droplet spatters produced in the first 5 layers of the L-PBF build using virgin and oxidised powders, and their corresponding D_{eq} values. It is evident that the virgin condition produced 2 to 4 times more droplet spatters than the oxidised

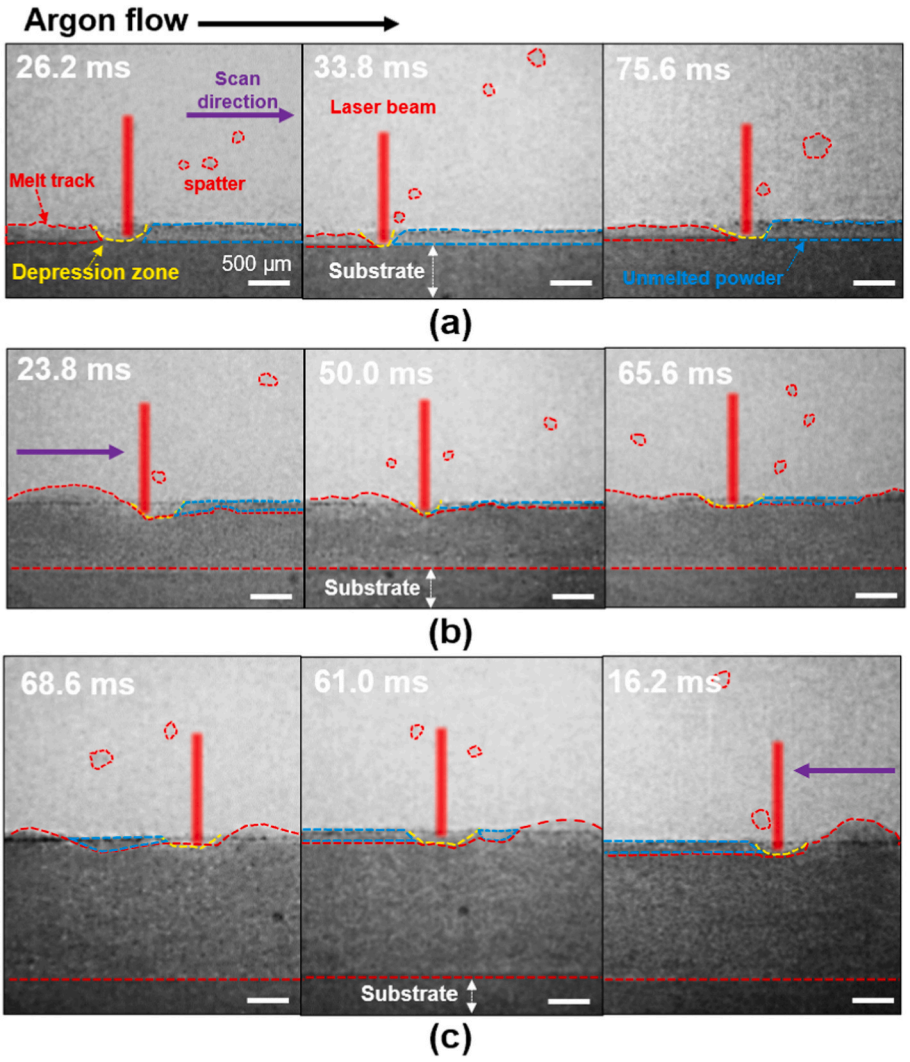

Fig. 2. Time series radiographs (and Supplementary videos 1–3) showing laser-matter interaction and spatter formation during L-PBF of virgin Ti6Al4V powder at 150 W and 50 mm s $^{-1}$ at Layer (a) 1, (b) 5 and (c) 10, respectively. The scale bars in all radiographs are 500 μm. Red-dashed circle marks the spatter contours; the contours of melt tracks, unmelted powder and the depression regions are marked by red, blue and yellow-dashed lines, respectively. (For interpretation of the references to colour in this figure legend, the reader is referred to the Web version of this article.)

condition within the first 5 layers. The largest equivalent diameter range of the droplet spatters was almost four times higher (120–150 μm) compared to the $D_v(50)$ of the powder bed particles (~38 μm).

3.4. Effects of spatter on build and powder layer properties

Fig. 5a and b shows that spatters can fall back into the melting region and may deposit over the previously formed melt track, increasing the melt track surface roughness (Fig. 5a). Some spatter may entrain into the molten pool as shown in Fig. 5b (highlighted by the red-dashed circle). Depending on the processing parameters, the spatter size and its chemical composition, these embedded un-melted spatters can undergo melting/re-melting with laser irradiation or remain un-melted, then act as stress concentration sites for fatigue crack initiation.

Fig. 5c shows a droplet spatter ejected from the laser-matter interaction zone, and it subsequently landed on a powder particle, merged, and then solidified. Fig. 5d–e shows spatter-induced powder agglomerates that occurred either due to the bombardment of droplet spatter with the surrounding particles during ejection or when the ejected droplet spatter fell back in the unfused area of the powder bed. Fig. 5f shows a 'super-ball' spatter particle, *i.e.,* a liquid spatter that became solidified during its flight into a large spherical particle (~90 μm). We also observed liquid-liquid (Fig. 5g) and liquid-solid (Fig. 5h) spatter agglomerations under non-optimised parameters (100 W and 50 mms^{-1}). Fig. 5g shows a small slow-moving spatter coalesced with another spatter to form a larger droplet spatter. Fig. 5h shows a large spatter could be formed by coalescing a droplet spatter (red-dashed circle) with powder spatter (purple circle).

3.5. Melt track surface analysis

The top-surface profile of the melt tracks of the virgin and oxidised builds are shown in Fig. 6a and b respectively. The undulations (*i.e.* frequency and amplitude) present on the melt track surfaces along the track length in both conditions were higher in the virgin condition compared to the oxidised condition.

The surface roughness, R_a, of the previously solidified melt tracks causes variation in the layer thickness during multilayer L-PBF builds. Each division in the Y-axis corresponds to the pre-set layer thickness of 100 μm. The actual layer height varied significantly from the user-defined layer thickness, along the track length. In the virgin condition, the layer height increased to a maximum of 260 μm in the largest valley region and reduced to 30 μm at the highest hump region. In the oxidised condition, the layer height varied between 30 μm and 152 μm: relatively less variation in actual layer height compared to that of the virgin condition.

The R_a values at the top surfaces of each melt track was measured based on the X–Y coordinates of the melt track boundaries (see method in Section 2.6). Fig. 6c compares the R_a values of the 10-layer builds produced from the virgin and oxidised powders. The melt tracks formed from the virgin powder had a higher R_a than oxidised builds in all built layers. Under both conditions, the R_a increased steeply in the first few

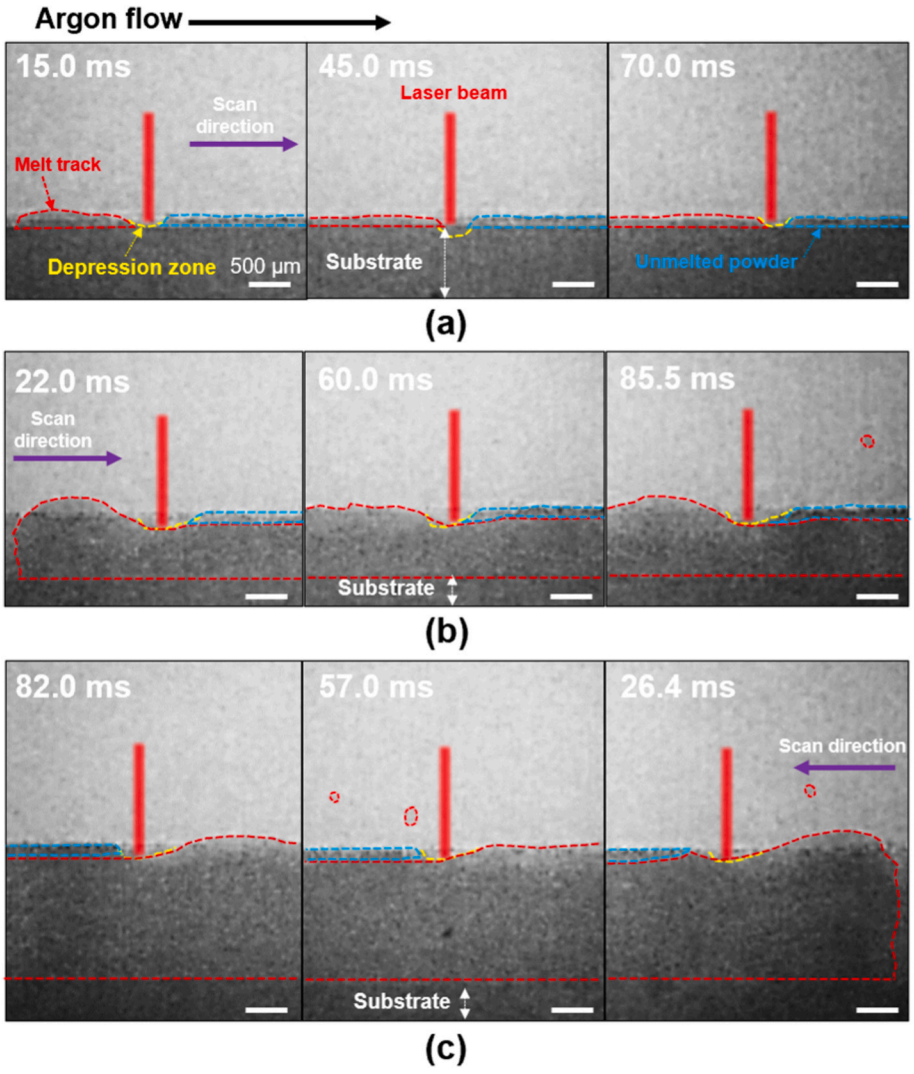

Fig. 3. Time series images (and Supplementary Videos 4–6) showing laser-matter interaction and spatter formation during L-PBF of oxidised Ti6Al4V powder at 150 W and 50 mm s $^{-1}$ at Layer (a) 1, (b) 5 and (c) 10, respectively. The scale bars in all radiographs are 500 μm. Red-dashed circle marks the spatter contours; the contours of melt tracks, unmelted powder and the depression regions are marked by red, blue, and yellow-dashed lines, respectively. (For interpretation of the references to colour in this figure legend, the reader is referred to the Web version of this article.)

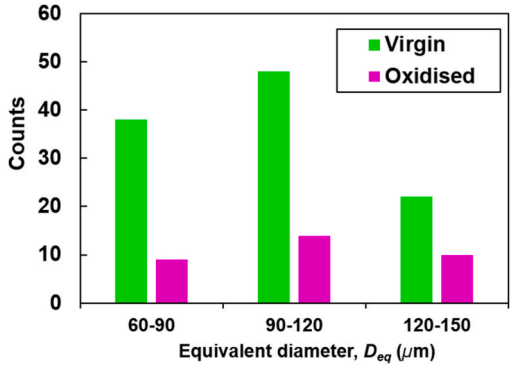

Fig. 4. Number of droplet spatter quantified during L-PBF of virgin and oxidised conditions for the first 5 layers of a 10-layer build.

layers and then stabilised with marginal fluctuations between each layer.

Since measuring surface roughness using X-ray radiographs is neither a standard method nor followed commonly in industry, the surface roughness of the final layer (10th layer) in the virgin and oxidised builds was measured according to ISO 4288. The R_a value was 14 μm for the virgin build and 3 μm for the oxidised build. The corresponding R_a values measured from X-ray radiographs were 29 μm and 13 μm for the virgin and oxidised builds, respectively. The difference in the measured R_a values between the two techniques can be attributed to their resolvable spatial resolution and measurement methods. Both results show that the melt tracks produced from the virgin powder were rougher than those made from the oxidised powder.

3.6. Post-mortem analysis

XCT was used to further analyse the defect distribution and morphology in the virgin and oxidised builds, see Fig. 7. The pores were randomly distributed in both builds (Fig. 7a and b) and their equivalent diameter ranged from 10 to 100 μm. Fig. 7c shows that the virgin build contained ~9 times more porosity (%) compared to the oxidised builds. Fig. 7d shows that pores are mostly spherical in both conditions. A small fraction (<0.003%) of low-sphericity large-size pores (50–80 μm) in the oxidised condition can correspond to a minor fraction of high-aspect-ratio pores present at the end of the scan track (Fig. 7b) which could be due to elongated pore formed during laser turning [3]. We speculate that these pores were formed due to the reduction in the laser scan speed towards the end of the scan vector, as the skywriting settings were not used in our experiments, leading to the formation of keyhole pores and their coalescence.

Fig. 8 shows the microstructure of virgin and oxidised builds in the build direction. Both samples exhibit a typical L-PBF Ti6Al4V microstructure consisting of predominantly α'. As expected, an increase in

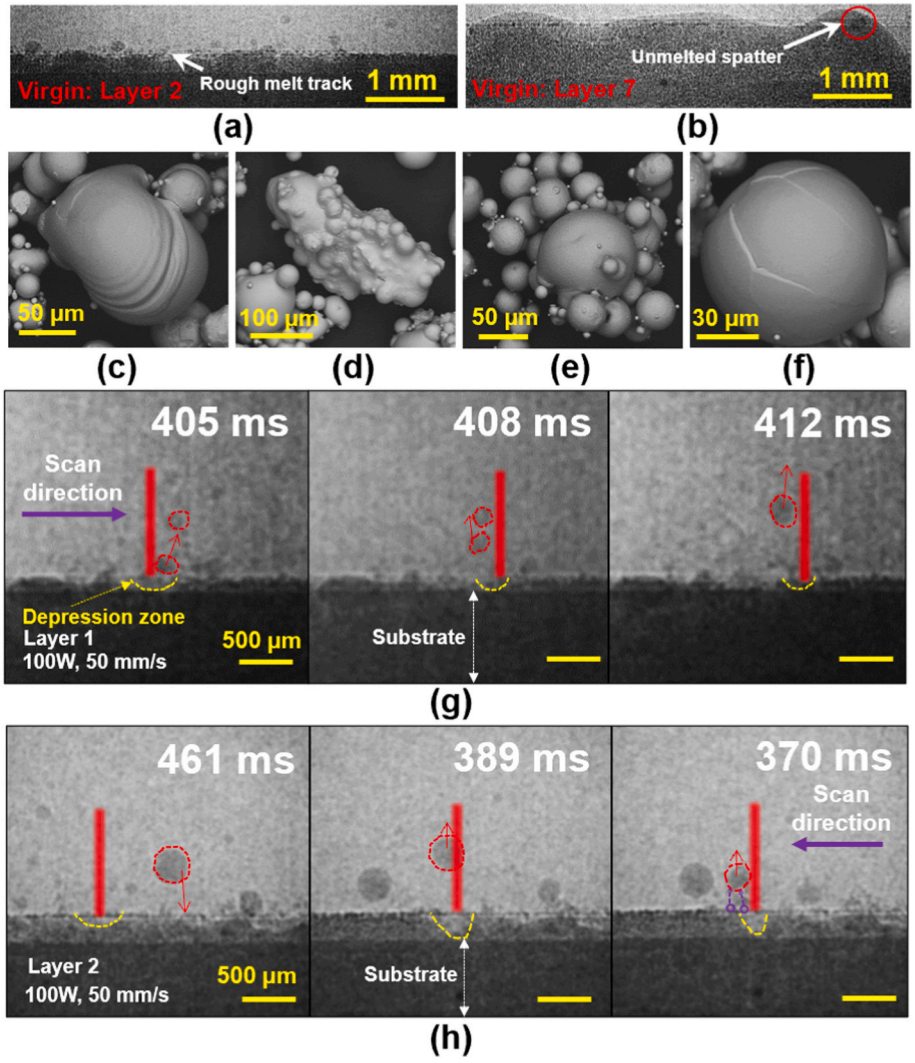

Fig. 5. (a) A radiograph of Layer 2 virgin build formed using 100 W laser power and 50 mm s^{-1} scan speed showing spatter-induced surface roughness; (b) a radiograph of Layer 7 virgin build produced using 150 W laser power and 50 mm s^{-1} scan speed showing unmelted spatter (red circle). Powder bed contamination by droplet spatters: spatter solidified/sintered over a (c) single powder particle, (d and e) spatter agglomerates of particles with different aspect ratios, and (f) spherical 'super-ball' spatter. Time-series radiographs showing Layer 1 and 2 in virgin condition at 100 W and 50 mm s^{-1}: (g) coalescence of one droplet spatter with another and (h) coalescence of powder spatters with a droplet spatter to form a large spatter. The droplet spatters are indicated by red circles while powder spatters are indicated by purple circles respectively. (For interpretation of the references to colour in this figure legend, the reader is referred to the Web version of this article.)

Vickers microhardness measurements from 393 ± 10 HV for the virgin to 461 ± 8 HV for the oxidised builds was observed.

4. Discussion

Increasing oxygen content of the recycled Ti6Al4V powder is found to be the major factor limiting the number of times that the Ti6Al4V powder can be recycled. Our work uses *in situ* X-ray imaging to understand, reveal, and evaluate the effects of powder oxidation on process and defect dynamics that occur during L-PBF processing of multi-layer virgin and highly oxidised Ti6Al4V powders.

4.1. Spatter dynamics

During L-PBF, two types of melt ejections, *i.e.,* powder and droplet spatters, were commonly observed from the laser-matter interaction zone: (1) solid powder spatter (powder particle ejection) and (2) droplet spatter (melt ejections) [46]. Solid powder spatters occur at the region surrounding the melt pool due to the entrainment of unfused powder particles into the metal vapour jet [47] and droplet spatters eject from the melt pool surface due to the strong exertion of recoil pressure on the melt pool surface.

Fig. 5a-f show that spatters with or without agglomerated with other powder particles, are generally coarser than the virgin powder, *i.e.,* twice the size of the parent powder particles. Although most spatters can be filtered out from the subsequent builds during sieving when the powder is recycled, some high-aspect-ratio spatter agglomerates (Fig. 5d) can pass through sieves in certain orientations and end up in the powder layer, affecting powder flow and packing density.

Oxidised spatter particles can also occur leading to chemical inhomogeneity of the powder layer when they fall back into the powder bed [29,48]. The amount of droplet spatter could be influenced by the processing parameters like input energy density [49], chamber pressure and oxygen content [50]. Our results show that the number of spatters produced in the virgin condition (Fig. 2 and Supplementary Videos 1-3) was ~4 times higher than that in the oxidised condition (Fig. 3 and Supplementary videos 4-6). The processing conditions or linear energy density (LED) applied for both powders were the same, therefore, the difference in the spatter quantity can only be attributed to the variation in the oxygen content of the Ti6Al4V powder.

The oxide layer at the powder surface altered three phenomena that resulted in a reduction of spatters for the condition studied. Firstly, the oxidised Ti6Al4V powder has shown enrichment of aluminium on its surface, *i.e.* there is a preferential formation of aluminium oxide (up to 60 nm depth) [51]. Due to the presence of aluminium oxide, the oxidised Ti6Al4V powder is expected to have a lower laser absorption at the 1070 nm wavelength [52]. Reduction in laser absorption (~2 times) of the oxidised powder (Fig. 1f) decreases the LED input onto the powder bed, possibly resulting in conduction mode, less turbulence in the melt flow, metal vaporisation, thereby, reducing melt ejections.

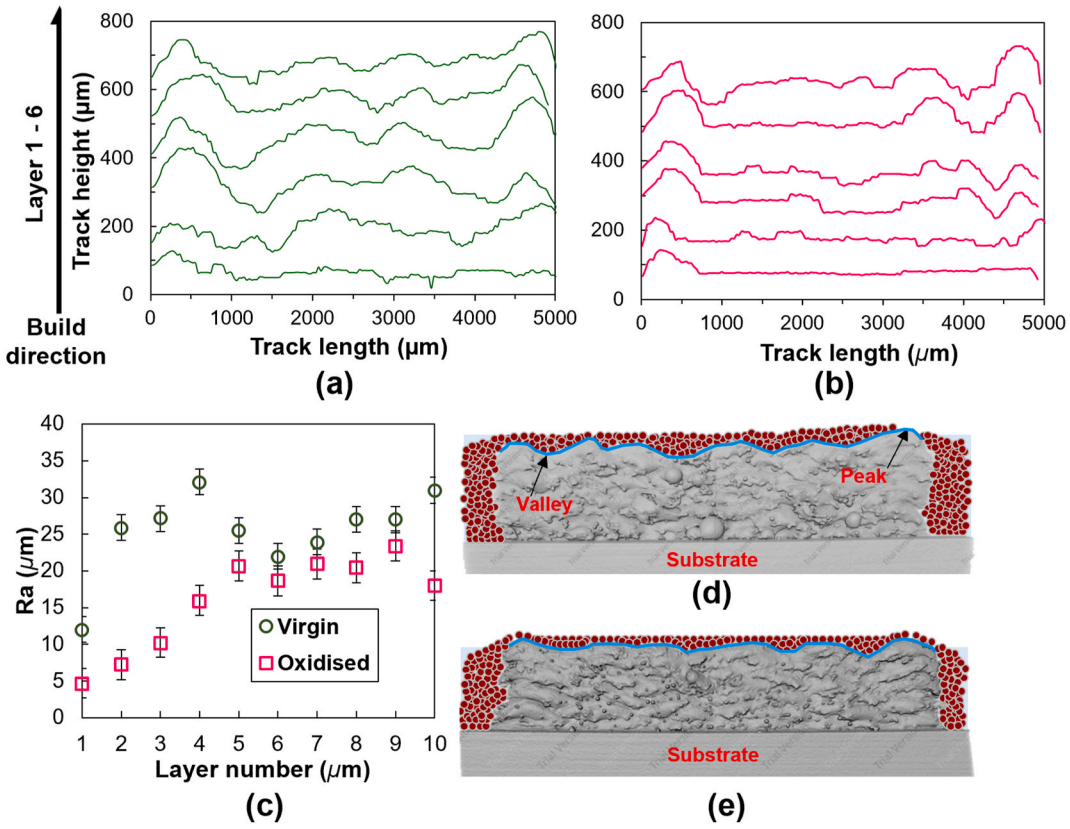

Fig. 6. Surface profiles of L-PBF builds produced by (a) virgin and (b) oxidised powder from layers 1 to 6; (c) average and standard deviations of surface roughness, R_a, measurements in virgin and oxidised builds; illustration showing the effect of layer roughness on powder spreading in (d) virgin and (e) oxidised conditions, where the red circle represents the powder particles and the grey colour objects are the XCT rendered thin wall build. (For interpretation of the references to colour in this figure legend, the reader is referred to the Web version of this article.)

Secondly, the presence of oxides in the melt pool as surface-active elements can alter the temperature-dependent surface tension gradient from negative to positive, similar to the observations reported in Ref. [53], and thereby reverse the Marangoni convection from outward centrifugal to inward centripetal flow. The reversal of melt flow direction also increases the melt depth, which has been widely observed in different processes, *e.g.* arc welding of 316L [54], laser welding of stainless steel [55], direct energy deposition (DED) of Ti6242 [36], and in L-PBF of Invar 36 powder [37]. In those studies, some amount of oxygen remained insoluble as oxides on the melt pool surface, altering the surface tension gradient and thereby, Marangoni convection. In contrast, the solubility of oxygen in Ti melt is known to be high., it can accept up to 66 at.% oxygen and upon cooling, up to 33 at.% oxygen based on the Ti–O phase diagram [56]. Furthermore, the melting and boiling points of TiO_2 (1843 °C and 2972 °C respectively) and Al_2O_3 (2072 °C and 2977 °C respectively) are higher than the melting point of Ti6Al4V (1668 °C), the temperatures experienced during L-PBF are likely to surpass these temperatures [25], therefore, the surface oxides could be dissociated as oxygen species into the melt pool. The dissolved oxygen can increase the viscosity of the melt pool >2 times when the oxygen level increases from 0.04 wt% to 0.09 wt% and hence the viscosity of the Ti6Al4V melt pool with 0.40 wt% oxygen is expected to be substantially higher than that reported by Ref. [57].

An increase in the viscosity of the melt pool is another factor that reduces turbulence in the melt pool because viscous shear forces oppose the backward surge of the melt pool, reducing its flow inertia [58]. Since the flow inertia was greatly reduced and unable to overcome the surface tension of the melt pool, droplet spatters could not escape from the melt pool surface. This explains why the number of droplet spatters in the oxidised condition was ~4 times lower than that in the virgin condition. Similar observations were reported in Ref. [40] during laser melting of 13–93 bioactive glass [40] and SiO_2 powders [59], where the highly viscous melt pool produced fewer spatters. The abovementioned evolution mechanisms of melt pool, defects, and surface roughness in L-PBF of virgin and oxidised powders are summarised into Fig. 9a and b, respectively.

Thirdly, the topology of the melt track causes heterogeneity in powder layer thickness during multilayer build as shown in Fig. 6d and e. This means the normalised LED (normalised LED = LED/layer thickness) along the scan vector changes significantly. For example: The layer thickness was 230 μm in the large valley region and the normalised LED measured 13 J/mm^2, while the layer thickness in the highest hump region was only 30 μm and the normalised LED was 100 J/mm^2. More metal vaporisation can take place at high normalised LED and more likely to form spatters [50].

4.2. Surface roughness

The undulations formed on the melt track surfaces are commonly referred to as 'humps' in welding metallurgy, which are controlled by several factors including energy density, surface tension, viscous force, capillary force, recoil pressure, *etc.* [58,60]. Similar types of undulations have also been observed in Ti6Al4V virgin melt tracks produced by the L-PBF process in Ref. [35]. Nguyen et al. [61] identified that the major factor for the hump initiation was the strong backward momentum of the melt flow behind the energy source. Gunenthiram et al. [62] reported that the hump development is caused by the large aspect ratio of the melt tracks that promote Plateau-Rayleigh instability. Process simulation performed by Tang et al. [58] have shown that the formation of the first hump promotes the development of more humps as laser

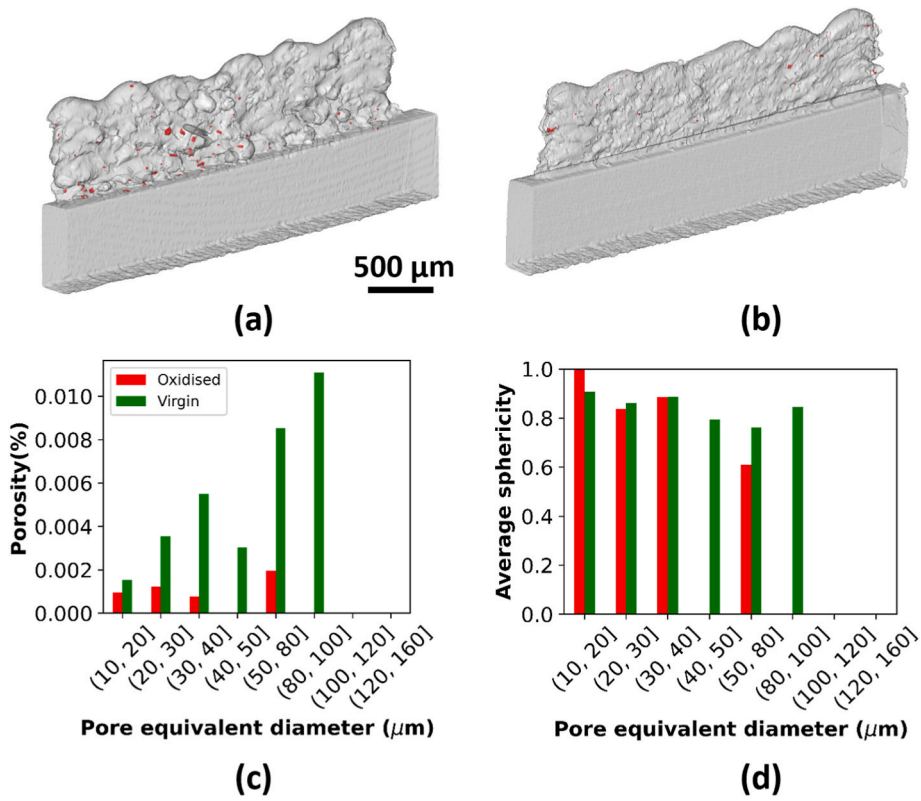

Fig. 7. Defect quantification using XCT in virgin and oxidised Ti6Al4V builds. 3D rendered XCT images of pores (red) overlaid on (a) virgin and (b) oxidised thin wall builds (grey). (c) Percentage of porosity and its (d) sphericity as a function of pore equivalent diameter. (For interpretation of the references to colour in this figure legend, the reader is referred to the Web version of this article.)

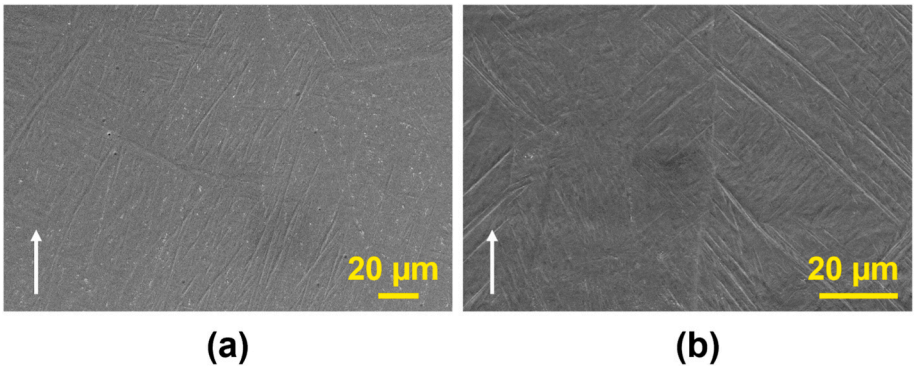

Fig. 8. Typical SEM images of (a) virgin and (b) oxidised build microstructures. White arrows indicate the build direction.

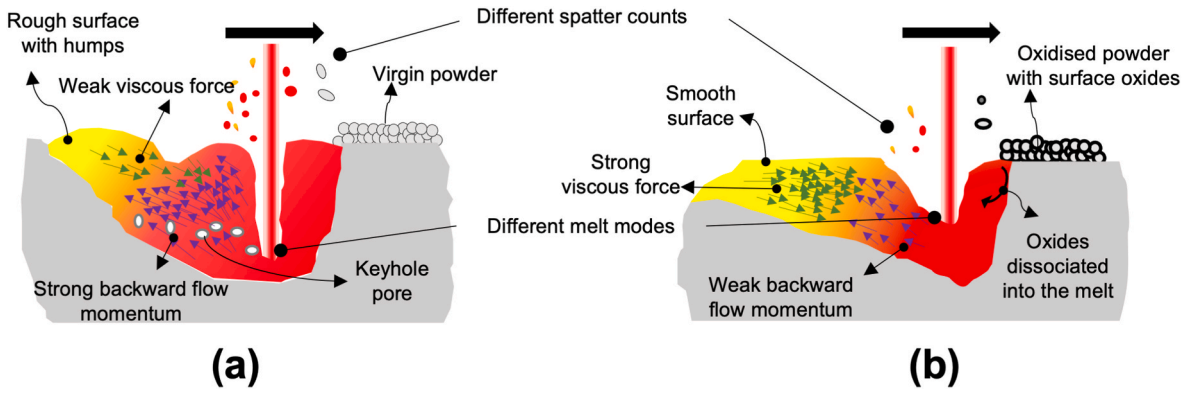

Fig. 9. Schematic representation of the vapour depression zone, melt pool and defect dynamics during L-PBF with (a) virgin and (b) oxidised powders.

track melting progresses, thereby leading to the formation of periodic humps along the melt track length, as shown in Fig. 6a and b. Leung et al. [38] hypothesised that the fast-flowing inert gas above the fast-flowing melt pool in the opposite direction can induce Kevin-Helmholtz instability that leads to the hump formation. A mathematical model developed in Ref. [58] also demonstrated that the backward flow inertia of the melt pool significantly reduced with an increase in viscous shear force, the oxidised powder produced a relatively more viscous melt pool than the virgin powder, had a low melt backward flow momentum, decreasing the undulations in the melt tracks (Fig. 9).

Since only single-track experiments were performed in the current investigation, a bi-directional scan strategy was employed; which generally provides a rougher surface. In commercial L-PBF machines, a wide range of scan strategies like island, helical, *etc.,* with optimum hatch distance and rotation in-between layers are commonly used to reduce surface roughness, and more importantly to prevent obstruction of the re-coater due to surface roughness causing build termination. Other methods include adjusting process parameters [63,64], laser re-melting [65,66], and post-process treatments [67] have also been investigated to reduce surface roughness. Our work shows that surface roughness can also be reduced by introducing oxygen in the powder feedstock.

4.3. Microstructural properties

Based on XCT analysis, the pore morphology and shape factor suggested that they are mostly gas and keyhole pores [19,68]. Gas pores are usually small with a high sphericity (>0.8) generated due to gas entrapment inside the melt pool from sources including Ar gas flow during L-PBF and powder feedstock. Keyhole pores are formed due to high energy input. The keyhole instability and keyhole collapse leave pores at the bottom regions of the melt pool. Keyhole pores are large with slightly lower roundness than gas pores [69,70]. The virgin build contains ~27 times more large-sized pores (%) (>40 μm) than the oxidised build (Fig. 7c and d), which are also with slightly lower sphericity compared to the small-sized pores that can be attributed to pores generated from keyhole fluctuations. The relatively high laser absorption (~2 times) in the virgin compared to the oxidised powder could have enabled the melting in the virgin condition to progress in the unstable keyhole process regime, promoting the formation of keyhole-induced pores (Fig. 9). Lastly, some high aspect ratio pores exhibited in the oxidised build at the end of the track were possibly due to pore formation during laser turning [71].

Leung et al. [37] showed that the inclusion of surface oxides into the melt pool of Invar 36 can act as pore nucleation sites causing more porosity to occur in the oxidised condition compared to the virgin condition. In contrast, our results on Ti6Al4V ascertain that the surface oxides broke down to elemental oxygen that was then dissolved in the melt pool. This is confirmed by the SEM results, wherein no undissolved oxides were found in the microstructural analysis, and the oxidised powder with oxygen content of up to 0.40 wt%, similar to that reported in electron beam powder bed fusion (E-PBF) of Ti6Al4V (with 0.46 wt% oxygen) [72] and no significant change in the microstructure was evident, similar observations were reported in Ref. [73] with 0.23 wt% oxygen in L-PBF of Ti6Al4V.

The oxidised melt pool with higher viscosity had sufficient wettability to form a uniform continuous layer with fewer lack-of-fusion defects, which was not the case in Ref. [40] with AM of 13–93 bioactive glass. Moreover, there is no correlation between defect distribution, variations in powder layer thickness at high input LED, *i.e.* the input LED was sufficient to prevent lack-of-fusion defects.

Our results show that the high oxygen content TiAl4V part exhibits 17% higher hardness than that the virgin part. At elevated temperatures, the dissolution of oxygen will first dissolve into the Ti matrix wherein the oxygen can occupy the octahedral interstitial (up to 34 at%) and cause strain in the *c*-axis of the hexagonal close-packed (hcp) crystal lattice [73,74]. Oxygen is also an alpha phase stabilising element in Ti6Al4V [73–75] and it tends to randomly segregate at the grain boundaries, acting as a solid solution strengthener, hindering the gliding of dislocations, leading to an intense hardening [73,75]. Detail hardening mechanism is reported in Ref. [76]. In general, an increase in oxygen will increase both yield strength and hardness in Ti and its alloys [73–76]. However, both virgin (0.12 wt% O) and oxidised powders (0.40 wt% O) were melted on a CP-Ti base plate; therefore, it is possible that the build can have a slightly lower oxygen content, compared to the powder due to the mixing or dilution effect as the laser can remelt the CP-Ti up to few layers of the build. Given that, both powders were processed under the same conditions, the dilution effect did not affect the mechanical properties.

Apart from process parameter optimisation, our study shows that surface modification of Ti6Al4V powder feedstock could alter laser absorption and subsequently the molten pool dynamics, improving the print quality of the L-PBF parts. However, further investigation of the tensile and fatigue properties would require assessing the detailed mechanical performance of the parts. Upon investigation, we can also question if the conventional 0.2 wt% O set as the maximum limit by ASTM on components produced by conventional manufacturing methods can hold true for AM in general.

5. Conclusions

This study investigated the effects of low (0.12 wt%) and high (0.40 wt%) oxygen content Ti6Al4V powder particles on laser-matter interaction during L-PBF using real-time synchrotron X-ray imaging coupled with a miniature L-PBF process replicator.

Key conclusions drawn from this study are as follows:

(i) We revealed the influence of powder oxidation during multilayer L-PBF of Ti6Al4V. We show that powder oxidation of Ti6Al4V with up to 0.40 wt% at a high LED can reduce porosity, the volume of droplet spatter, surface roughness, and enhance the microhardness of the build parts.
(ii) High oxygen content powder developed powder surface oxides that lowered laser absorption by half, and therefore reduced the energy input onto the powder bed during L-PBF. This increased the viscosity of the melt pool, resulting in a less vigorous melt flow, and hence fewer melt ejections.
(iii) The oxidised powder produced relatively smooth melt tracks compared to the virgin powder, this reduced uneven powder layer spreading in subsequent build layers and generation of melt ejections.
(iv) The virgin builds contained a larger number of spherical pores compared to the oxidised builds. The spherical pores are hypothesised to be keyhole pores owing to relatively larger size and high laser absorption during L-PBF, the increased turbulence flow in the virgin powder melt pool, and keyhole instability.
(v) The powder surface oxides are hypothesised to be dissociated into oxygen species during melting and solidification as no oxide residues were found in the microstructural analysis. The dissolved oxygen increased micro hardness of oxidised build by 17%.

CRediT authorship contribution statement

Gowtham Soundarapandiyan: Conceptualization, Data curation, Formal analysis, Investigation, Visualization, Writing – original draft. **Chu Lun Alex Leung:** Conceptualization, Data curation, Formal analysis, Funding acquisition, Investigation, Methodology, Project administration, Resources, Supervision, Visualization, Writing – original draft, Writing – review & editing. **Carol Johnston:** Project administration, Supervision, Writing – review & editing. **Bo Chen:** Data curation,

Investigation, Supervision, Writing – review & editing. **Raja H.U. Khan:** Resources, Supervision, Writing – review & editing. **Phil McNutt:** Methodology, Resources, Writing – review & editing. **Alisha Bhatt:** Investigation, Methodology. **Robert C. Atwood:** Resources, Supervision. **Peter D. Lee:** Conceptualization, Data curation, Funding acquisition, Methodology, Supervision, Writing – review & editing. **Michael E. Fitzpatrick:** Conceptualization, Resources, Funding acquisition, Supervision, Writing – review & editing.

Declaration of competing interest

The authors declare that they have no known competing financial interests or personal relationships that could have appeared to influence the work reported in this paper.

Data availability

Data will be made available on request.

Acknowledgements

This research was made possible by the sponsorship and support of the Lloyd's Register Foundation, a charitable organisation that helps to protect life and property by supporting engineering-related education, public engagement and the application of research. The work was enabled through and conducted at the National Structural Integrity Research Centre (NSIRC) managed by TWI through a network of both national and international Universities. The authors want to thank Diamond Light Source, UK for providing the beamtime (ref: MG2370). The authors acknowledge the XCT facility and analysis at the Research Complex at Harwell (RCaH), funded through the UK-EPSRC MAPP: Future Manufacturing Hub (EP/P006566/1), Manufacturing by Design (EP/W003333/1), and Made Smarter Innovation - Materials Made Smarter Research Centre (EP/V061798/1); Data-driven, Reliable, and Effective Additive Manufacturing using multi-BEAM technologies (EP/W037483/1) and other grants (EP/R511638/1, EP/I02249X/1 and EP/M009688/1)), and a Royal Academy of Engineering Chair in Emerging Technology (CiET1819/10). Bo Chen acknowledges financial supports through the EPSRC Early Career Fellowship Scheme EP/R043973/1.

Appendix A. Supplementary data

Supplementary data to this article can be found online at https://doi.org/10.1016/j.ijmachtools.2023.104049.

References

[1] Y. Kok, X.P. Tan, P. Wang, M.L.S. Nai, N.H. Loh, E. Liu, S.B. Tor, Anisotropy and heterogeneity of microstructure and mechanical properties in metal additive manufacturing: a critical review, Mater. Des. 139 (2018) 565–586, https://doi.org/10.1016/j.matdes.2017.11.021.

[2] C. Körner, Additive manufacturing of metallic components by selective electron beam melting - a review, Int. Mater. Rev. 61 (2016) 361–377, https://doi.org/10.1080/09506608.2016.1176289.

[3] C. Tan, F. Weng, S. Sui, Y. Chew, G. Bi, Progress and perspectives in laser additive manufacturing of key aeroengine materials, Int. J. Mach. Tool Manufact. 170 (2021), 103804, https://doi.org/10.1016/j.ijmachtools.2021.103804.

[4] R.J. Hebert, Viewpoint: metallurgical aspects of powder bed metal additive manufacturing, J. Mater. Sci. 51 (2016) 1165–1175, https://doi.org/10.1007/s10853-015-9479-x.

[5] K. Mumtaz, N. Hopkinson, Top surface and side roughness of Inconel 625 parts processed using selective laser melting, Rapid Prototyp. J. 15 (2009) 96–103, https://doi.org/10.1108/13552540910943397.

[6] K. Opatová, I. Zetková, L. Kučerová, Relationship between the size and inner structure of particles of virgin and re-used ms1 maraging steel powder for additive manufacturing, Materials 13 (2020), https://doi.org/10.3390/ma13040956.

[7] L.E. Murr, S.M. Gaytan, D.A. Ramirez, E. Martinez, J. Hernandez, K.N. Amato, P. W. Shindo, F.R. Medina, R.B. Wicker, Metal fabrication by additive manufacturing using laser and electron beam melting technologies, J. Mater. Sci. Technol. 28 (2012) 1–14, https://doi.org/10.1016/S1005-0302(12)60016-4.

[8] M. Colopi, L. Caprio, A.G. Demir, B. Previtali, Selective laser melting of pure Cu with a 1 kW single mode fiber laser, Procedia CIRP 74 (2018) 59–63, https://doi.org/10.1016/j.procir.2018.08.030.

[9] T.N. Aboulkhair, M. Simonelli, L. Parry, I. Ashcroft, C. Tuck, R. Hague, 3D printing of aluminium alloys: additive manufacturing of aluminium alloys using selective laser melting, Prog. Mater. Sci. 106 (2019), https://doi.org/10.1016/j.pmatsci.2019.100578.

[10] G. Soundarapandiyan, C. Johnston, R.H.U. Khan, B. Chen, M.E. Fitzpatrick, A technical review of the challenges of powder recycling in the laser powder bed fusion additive manufacturing process, J. Eng. 2021 (2021) 97–103, https://doi.org/10.1049/tje2.12013.

[11] A.T. Sutton, C.S. Kriewall, M.C. Leu, J.W. Newkirk, Powder characterisation techniques and effects of powder characteristics on part properties in powder-bed fusion processes, Virtual Phys. Prototyp. 12 (2017) 3–29, https://doi.org/10.1080/17452759.2016.1250605.

[12] H.P. Tang, M. Qian, N. Liu, X.Z. Zhang, G.Y. Yang, J. Wang, Effect of powder reuse times on additive manufacturing of Ti-6Al-4V by selective electron beam melting, JOM (J. Occup. Med.) 67 (2015) 555–563, https://doi.org/10.1007/s11837-015-1300-4.

[13] G. Soundarapandiyan, C. Johnston, R.H.U. Khan, C.L.A. Leung, P.D. Lee, E. Hernández-Nava, B. Chen, M.E. Fitzpatrick, The effects of powder reuse on the mechanical response of electron beam additively manufactured Ti6Al4V parts, Addit. Manuf. 46 (2021), 102101, https://doi.org/10.1016/j.addma.2021.102101.

[14] E. Santecchia, S. Spigarelli, M. Cabibbo, Material reuse in laser powder bed fusion: side effects of the laser—metal powder interaction, Metals 10 (2020), https://doi.org/10.3390/met10030341.

[15] F.J. Alamos, J. Schiltz, K. Kozlovsky, R. Attardo, C. Tomonto, T. Pelletiers, S. R. Schmid, Effect of powder reuse on mechanical properties of Ti-6Al-4V produced through selective laser melting, Int. J. Refract. Met. Hard Mater. 91 (2020), https://doi.org/10.1016/j.ijrmhm.2020.105273.

[16] L. Denti, A. Sola, S. Defanti, C. Sciancalepore, F. Bondioli, Effect of powder recycling in laser-based powder bed fusion of Ti-6Al-4V, Manuf. Technol. 19 (2019) 190–196, https://doi.org/10.21062/ujep/268.2019/a/1213-2489/mt/19/2/190.

[17] R. Harkin, H. Wu, S. Nikam, J. Quinn, S. McFadden, Reuse of grade 23 ti6al4v powder during the laser-based powder bed fusion process, Metals 10 (2020) 1–14, https://doi.org/10.3390/met10121700.

[18] V. Seyda, N. Kaufmann, C. Emmelmann, Investigation of aging processes of Ti-6Al-4V powder material in laser melting, Phys. Procedia 39 (2012) 425–431, https://doi.org/10.1016/j.phpro.2012.10.057.

[19] S. Tammas-Williams, P.J. Withers, I. Todd, P.B. Prangnell, The effectiveness of hot isostatic pressing for closing porosity in titanium parts manufactured by selective electron beam melting, Metall. Mater. Trans. A Phys. Metall. Mater. Sci. 47 (2016) 1939–1946, https://doi.org/10.1007/s11661-016-3429-3.

[20] G. Soundarapandiyan, R. Khan, C. Johnston, B. Chen, M. Fitzpatrick, Effect of postprocessing thermal treatments on electron-beam powder bed–fused Ti6Al4V, Mater. Des. Process. Commun. 3 (2021), https://doi.org/10.1002/mdp2.168.

[21] J.M. Oh, B.G. Lee, S.W. Cho, S.W. Lee, G.S. Choi, J.W. Lim, Oxygen effects on the mechanical properties and lattice strain of Ti and Ti-6Al-4V, Met. Mater. Int. 17 (2011) 733–736, https://doi.org/10.1007/s12540-011-1006-2.

[22] M. Yan, M.S. Dargusch, T. Ebel, M. Qian, A transmission electron microscopy and three-dimensional atom probe study of the oxygen-induced fine microstructural features in as-sintered Ti-6Al-4V and their impacts on ductility, Acta Mater. 68 (2014) 196–206, https://doi.org/10.1016/j.actamat.2014.01.015.

[23] L. Cordova, M. Campos, T. Tinga, Revealing the effects of powder reuse for selective laser melting by powder characterization, JOM (J. Occup. Med.) 71 (2019) 1062–1072, https://doi.org/10.1007/s11837-018-3305-2.

[24] T. Takahashi, Y. Minamino, H. Hirazawa, T. Ouchi, High-temperature oxidation and its kinetics study of Ti-6Al-4V alloys in air, Keikinzoku/Journal Japan Inst. Light Met. 66 (2016) 306–311, https://doi.org/10.2464/jilm.66.306.

[25] N. Derimow, N. Hrabe, Oxidation in reused powder bed fusion additive manufacturing Ti-6Al-4V feedstock: a brief review, Jom 73 (2021) 3618–3638, https://doi.org/10.1007/s11837-021-04872-y.

[26] Z. Li, H. Li, J. Yin, Y. Li, Z. Nie, X. Li, D. You, K. Guan, W. Duan, L. Cao, D. Wang, L. Ke, Y. Liu, P. Zhao, L. Wang, K. Zhu, Z. Zhang, L. Gao, L. Hao, A review of spatter in laser powder bed fusion additive manufacturing: in situ detection, generation, effects, and countermeasures, Micromachines 13 (2022), https://doi.org/10.3390/mi13081366.

[27] D. Wang, S. Wu, F. Fu, S. Mai, Y. Yang, Y. Liu, C. Song, Mechanisms and characteristics of spatter generation in SLM processing and its effect on the properties, Mater. Des. 117 (2017) 121–130, https://doi.org/10.1016/j.matdes.2016.12.060.

[28] P.E. Carrion, A. Soltani-Tehrani, N. Phan, N. Shamsaei, Powder recycling effects on the tensile and fatigue behavior of additively manufactured Ti-6Al-4V parts, JOM (J. Occup. Med.) 71 (2019) 963–973, https://doi.org/10.1007/s11837-018-3248-7.

[29] R. Williams, M. Bilton, N. Harrison, P. Fox, The impact of oxidised powder particles on the microstructure and mechanical properties of Ti-6Al-4 V processed by laser powder bed fusion, Addit. Manuf. 46 (2021), 102181, https://doi.org/10.1016/j.addma.2021.102181.

[30] C.L.A. Leung, S. Marussi, R.C. Atwood, P.D. Lee, M. Towrie, P.J. Withers, In situ X-ray imaging of defect and molten pool dynamics in laser additive manufacturing, Nat. Commun. 9 (2018), https://doi.org/10.1038/s41467-018-03734-7.

[31] Q. Guo, M. Qu, L.I. Escano, S.M.H. Hojjatzadeh, Z. Young, K. Fezzaa, L. Chen, Revealing melt flow instabilities in laser powder bed fusion additive manufacturing of aluminum alloy via in-situ high-speed X-ray imaging, Int. J. Mach. Tool

Manufact. 175 (2022), 103861, https://doi.org/10.1016/j.ijmachtools.2022.103861.
[32] Y. Huang, T.G. Fleming, S.J. Clark, S. Marussi, K. Fezzaa, J. Thiyagalingam, C.L. A. Leung, P.D. Lee, Keyhole fluctuation and pore formation mechanisms during laser powder bed fusion additive manufacturing, Nat. Commun. 13 (2022) 1–11, https://doi.org/10.1038/s41467-022-28694-x.
[33] R. Cunningham, S.P. Narra, C. Montgomery, J. Beuth, A.D. Rollett, Synchrotron-based X-ray microtomography characterization of the effect of processing variables on porosity formation in laser power-bed additive manufacturing of Ti-6Al-4V, Jom 69 (2017) 479–484, https://doi.org/10.1007/s11837-016-2234-1.
[34] H. Ghasemi-Tabasi, C. de Formanoir, S. Van Petegem, J. Jhabvala, S. Hocine, E. Boillat, N. Sohrabi, F. Marone, D. Grolimund, H. Van Swygenhoven, R.E. Logé, Direct observation of crack formation mechanisms with operando Laser Powder Bed Fusion X-ray imaging, Addit. Manuf. 51 (2022), https://doi.org/10.1016/j.addma.2022.102619, 0–10.
[35] L. Sinclair, C.L.A. Leung, S. Marussi, S.J. Clark, Y. Chen, M.P. Olbinado, A. Rack, J. Gardy, G.J. Baxter, P.D. Lee, In situ radiographic and ex situ tomographic analysis of pore interactions during multilayer builds in laser powder bed fusion, Addit. Manuf. 36 (2020), https://doi.org/10.1016/j.addma.2020.101512.
[36] C. Iantaffi, C.L.A. Leung, Y. Chen, S. Guan, R.C. Atwood, J. Lertthanasarn, M.-S. Pham, M. Meisnar, T. Rohr, P.D. Lee, Oxidation induced mechanisms during directed energy deposition additive manufactured titanium alloy builds, Addit. Manuf. Lett. 1 (2021), 100022, https://doi.org/10.1016/j.addlet.2021.100022.
[37] C.L.A. Leung, S. Marussi, M. Towrie, R.C. Atwood, P.J. Withers, P.D. Lee, The effect of powder oxidation on defect formation in laser additive manufacturing, Acta Mater. 166 (2019) 294–305, https://doi.org/10.1016/j.actamat.2018.12.027.
[38] C.L.A. Leung, D. Luczyniec, S. Marussi, E. Guo, R.C. Atwood, M. Meisnar, B. Saunders, P.D. Lee, Quantification of interdependent dynamics during laser additive manufacturing Using X-ray imaging informed multi-physics and multiphase simulation, Adv. Sci. 9 (36) (2022) 2203546, https://doi.org/10.1002/advs.202203546.
[39] V.V. Popov, A. Katz-Demyanetz, A. Garkun, M. Bamberger, The effect of powder recycling on the mechanical properties and microstructure of electron beam melted Ti-6Al-4 V specimens, Addit. Manuf. 22 (2018) 834–843, https://doi.org/10.1016/j.addma.2018.06.003.
[40] C.L.A. Leung, S. Marussi, M. Towrie, J. del Val Garcia, R.C. Atwood, A.J. Bodey, J. R. Jones, P.J. Withers, P.D. Lee, Laser-matter interactions in additive manufacturing of stainless steel SS316L and 13-93 bioactive glass revealed by in situ X-ray imaging, Addit. Manuf. 24 (2018) 647–657, https://doi.org/10.1016/j.addma.2018.08.025.
[41] C.L.A. Leung, R. Tosi, E. Muzangaza, S. Nonni, P.J. Withers, P.D. Lee, Effect of preheating on the thermal, microstructural and mechanical properties of selective electron beam melted Ti-6Al-4V components, Mater. Des. 174 (2019), https://doi.org/10.1016/j.matdes.2019.107792.
[42] G. Jacob, C.U. Brown, M.A. Donmez, S.S. Watson, J. Slotwinski, Effects of Powder Recycling on Stainless Steel Powder and Built Material Properties in Metal Powder Bed Fusion Processes, 2017, https://doi.org/10.6028/NIST.AMS.100-6. Gaithersburg, MD.
[43] G. Lutjering, J.C. Williams, Titanium, Springer-Verlag Berlin Heidelberg, 2007, https://doi.org/10.1007/978-3-540-73036-1.
[44] S. Ly, A.M. Rubenchik, S.A. Khairallah, G. Guss, M.J. Matthews, Metal vapor micro-jet controls material redistribution in laser powder bed fusion additive manufacturing, Sci. Rep. 7 (2017) 1–12, https://doi.org/10.1038/s41598-017-04237-z.
[45] Z.A. Young, Q. Guo, N.D. Parab, C. Zhao, M. Qu, L.I. Escano, K. Fezzaa, W. Everhart, T. Sun, L. Chen, Types of spatter and their features and formation mechanisms in laser powder bed fusion additive manufacturing process, Addit. Manuf. 36 (2020), https://doi.org/10.1016/j.addma.2020.101438.
[46] Y. Liu, Y. Yang, S. Mai, D. Wang, C. Song, Investigation into spatter behavior during selective laser melting of AISI 316L stainless steel powder, JMADE 87 (2015) 797–806, https://doi.org/10.1016/j.matdes.2015.08.086.
[47] S.A. Khairallah, A.T. Anderson, A. Rubenchik, W.E. King, Laser powder-bed fusion additive manufacturing: physics of complex melt flow and formation mechanisms of pores, spatter, and denudation zones, Acta Mater. 108 (2016) 36–45, https://doi.org/10.1016/j.actamat.2016.02.014.
[48] A.T. Sutton, C.S. Kriewall, M.C. Leu, J.W. Newkirk, Powders for additive manufacturing processes: characterisation techniques and effects on part properties, in: Solid Free, Fabr., 2016.
[49] C. Qiu, C. Panwisawas, M. Ward, H.C. Basoalto, J.W. Brooks, M.M. Attallah, On the role of melt flow into the surface structure and porosity development during selective laser melting, Acta Mater. 96 (2015) 72–79, https://doi.org/10.1016/j.actamat.2015.06.004.
[50] Q. Guo, C. Zhao, L.I. Escano, Z. Young, L. Xiong, K. Fezzaa, W. Everhart, B. Brown, T. Sun, L. Chen, Transient dynamics of powder spattering in laser powder bed fusion additive manufacturing process revealed by in-situ high-speed high-energy x-ray imaging, Acta Mater. 151 (2018) 169–180, https://doi.org/10.1016/j.actamat.2018.03.036.
[51] A. Raza, C. Pauzon, S. Dubiez-Le Goff, E. Hryha, Effect of processing gas on spatter generation and oxidation of TiAl6V4 alloy in laser powder bed fusion process, Appl. Surf. Sci. 613 (2023), 156089, https://doi.org/10.1016/j.apsusc.2022.156089.
[52] B. Brandau, A. Da Silva, C. Wilsnack, F. Brueckner, A.F.H. Kaplan, Absorbance study of powder conditions for laser additive manufacturing, Mater. Des. 216 (2022), 110591, https://doi.org/10.1016/j.matdes.2022.110591.
[53] K.C. Mills, A. Shirali, Marangoni effects in welding, Philos. Trans. R. Soc. 356 (1998) 911–925, https://doi.org/10.1098/rsta.1998.0196.
[54] S. Lu, H. Fujii, H. Sugiyama, M. Tanaka, K. Nogi, Weld Penetration and Marangoni Convection with Oxide Fluxes in GTA Welding, 2002.
[55] C.R. Heiple, J.R. Rope, R.T. Stagner, R.J. Aden, Surface active element effects on the shape of gta, laser, and electron beam welds, Weld. J. (Miami, Fla) 62 (1983) 72–77.
[56] P.F. Chauvy, P. Hoffmann, D. Landolt, Electrochemical micromachining of titanium using laser oxide film lithography: excimer laser irradiation of anodic oxide, Appl. Surf. Sci. 211 (2003) 113–127, https://doi.org/10.1016/S0169-4332(03)00256-3.
[57] M. Skalon, B. Meier, T. Leitner, S. Arneitz, S.T. Amancio-Filho, C. Sommitsch, Reuse of Ti6al4V powder and its impact on surface tension, melt pool behavior and mechanical properties of additively manufactured components, Materials 14 (2021) 1–22, https://doi.org/10.3390/ma14051251.
[58] C. Tang, K.Q. Le, C.H. Wong, Physics of humping formation in laser powder bed fusion, Int. J. Heat Mass Tran. 149 (2020), https://doi.org/10.1016/j.ijheatmasstransfer.2019.119172.
[59] C.L.A. Leung, I. Elizarova, M. Isaacs, S. Marathe, E. Saiz, P.D. Lee, Enhanced near-infrared absorption for laser powder bed fusion using reduced graphene oxide, Appl. Mater. Today 23 (2021), 101009, https://doi.org/10.1016/j.apmt.2021.101009.
[60] D. Wu, X. Hua, D. Ye, F. Li, Understanding of humping formation and suppression mechanisms using the numerical simulation, Int. J. Heat Mass Tran. 104 (2017) 634–643, https://doi.org/10.1016/j.ijheatmasstransfer.2016.08.110.
[61] T.C. Nguyen, D.C. Weckman, D.A. Johnson, H.W. Kerr, The humping phenomenon during high speed gas metal arc welding, Sci. Technol. Weld. Join. 10 (2005) 447–459, https://doi.org/10.1179/174329305X44134.
[62] V. Gunenthiram, P. Peyre, M. Schneider, M. Dal, F. Coste, I. Koutiri, R. Fabbro, Experimental analysis of spatter generation and melt-pool behavior during the powder bed laser beam melting process, J. Mater. Process. Technol. 251 (2018) 376–386, https://doi.org/10.1016/j.jmatprotec.2017.08.012.
[63] Y. Tian, D. Tomus, P. Rometsch, X. Wu, Influences of processing parameters on surface roughness of Hastelloy X produced by selective laser melting, Addit. Manuf. 13 (2017) 103–112, https://doi.org/10.1016/j.addma.2016.10.010.
[64] M.F. Sadali, M.Z. Hassan, F. Ahmad, H. Yahaya, Z.A. Rasid, Influence of selective laser melting scanning speed parameter on the surface morphology, surface roughness, and micropores for manufactured Ti6Al4V parts, J. Mater. Res. 35 (2020) 2025–2035, https://doi.org/10.1557/jmr.2020.84.
[65] W. Yu, S.L. Sing, C.K. Chua, X. Tian, Influence of re-melting on surface roughness and porosity of AlSi10Mg parts fabricated by selective laser melting, J. Alloys Compd. 792 (2019) 574–581, https://doi.org/10.1016/j.jallcom.2019.04.017.
[66] K. Alrbaey, D. Wimpenny, R. Tosi, W. Manning, A. Moroz, On optimization of surface roughness of selective laser melted stainless steel parts: a statistical study, J. Mater. Eng. Perform. 23 (2014) 2139–2148, https://doi.org/10.1007/s11665-014-0993-9.
[67] A. Lamikiz, J.A. Sánchez, L.N. López de Lacalle, J.L. Arana, Laser polishing of parts built up by selective laser sintering, Int. J. Mach. Tool Manufact. 47 (2007) 2040–2050, https://doi.org/10.1016/j.ijmachtools.2007.01.013.
[68] S. Tammas-Williams, P.J. Withers, I. Todd, P.B. Prangnell, The influence of porosity on fatigue crack initiation in additively manufactured titanium components, Sci. Rep. 7 (2017), https://doi.org/10.1038/s41598-017-06504-5.
[69] R. Snell, S. Tammas-Williams, L. Chechik, A. Lyle, E. Hernández-Nava, C. Boig, G. Panoutsos, I. Todd, Methods for rapid pore classification in metal additive manufacturing, Jom 72 (2020) 101–109, https://doi.org/10.1007/s11837-019-03761-9.
[70] S.J. Wolff, H. Wang, B. Gould, N. Parab, Z. Wu, C. Zhao, A. Greco, T. Sun, In situ X-ray imaging of pore formation mechanisms and dynamics in laser powder-blown directed energy deposition additive manufacturing, Int. J. Mach. Tool Manufact. 166 (2021), 103743, https://doi.org/10.1016/j.ijmachtools.2021.103743.
[71] A.A. Martin, N.P. Calta, S.A. Khairallah, J. Wang, P.J. Depond, A.Y. Fong, V. Thampy, G.M. Guss, A.M. Kiss, K.H. Stone, C.J. Tassone, J. Nelson Weker, M. F. Toney, T. van Buuren, M.J. Matthews, Dynamics of pore formation during laser powder bed fusion additive manufacturing, Nat. Commun. 10 (2019), https://doi.org/10.1038/s41467-019-10009-2.
[72] W.A. Grell, E. Solis-Ramos, E. Clark, E. Lucon, E.J. Garboczi, P.K. Predecki, Z. Loftus, M. Kumosa, Effect of powder oxidation on the impact toughness of electron beam melting Ti-6Al-4V, Addit. Manuf. 17 (2017) 123–134, https://doi.org/10.1016/j.addma.2017.08.002.
[73] L. Tang, J. Fan, H. Kou, B. Tang, J. Li, Effect of oxygen variation on high cycle fatigue behavior of Ti-6Al-4V titanium alloy, Materials 13 (2020), https://doi.org/10.3390/ma13173858.
[74] B. Sun, S. Li, H. Imai, J. Umeda, K. Kondoh, Oxygen solid solution strengthened pure titanium powder materials, Join. Weld. Res. Inst. 41 (2012) 59–64, https://ir.library.osaka-u.ac.jp/repo/ouka/all/88074/32702_Abstract.pdf.
[75] T. Sugahara, D.A.P. Reis, C. de Moura Neto, M.J.R. Barboza, E.A.C. Perez, The effect of widmanstätten and equiaxed microstructures of Ti-6Al-4V on the oxidation rate and creep behavior, Mater. Sci. Forum 636–637 (2010) 657–662, https://doi.org/10.4028/www.scientific.net/msf.636-637.657.
[76] Z. Liu, G. Welsch, Effects of oxygen and heat treatment on the mechanical properties of alpha and beta titanium alloys, Metall. Trans. A 19 (1988) 527–542, https://doi.org/10.1007/BF02649267.